



Article

# Offline Diagnostics of Skin Sea Surface Temperature from a Prognostic Scheme and Its Application in Typhoon Forecasting Using the CMA-TRAMS Model over South China

**Yanxia Zhang** \*, **Daosheng Xu**, **Zitong Chen** and **Weiguang Meng**

Guangzhou Institute of Tropical and Marine Meteorology/Guangdong Provincial Key Laboratory of Regional Numerical Weather Prediction, CMA, Guangzhou No. 312 Dongguanzhuang Road, TianHe District, Guangzhou 510641, China

\* Correspondence: yxzhang@gd121.cn

**Abstract:** In the Tropical Regional Atmospheric Model System of South China of the China Meteorological Administration (CMA-TRAMS), the skin sea surface temperature ( $T_s$ ) remains fixed during the forecast time. This limits the model's performance in describing interactions between air and sea. The offline diagnostics and online analysis coupled with the CMA-TRAMS of  $T_s$  prognostic scheme were discussed. The results of the offline diagnostics showed that the profile shape parameter,  $\nu$ , and initial temperature,  $T_b$ , were sensitive to the forecasted  $T_s$ . Based on our observations, when  $\nu$  was set to 0.2 and  $T_b$  was the averaged  $T_s$  without obvious diurnal variation, the forecasted  $T_s$  was relatively reasonable. The forecasted  $T_s$  of CMA-TRAMS after coupling with the  $T_s$  scheme had diurnal variations during the overall forecast time, which was different from the fixed  $T_s$  from the uncoupled model. There existed a certain difference of forecasted  $T_s$  between uncoupled and coupled models in those days influenced by typhoons. The biases and Root Mean Square Errors (RMSEs) for the temperature and moisture in the lower layer and those for the wind speed in most layers were reduced and, therefore, the accuracy of environmental field forecasting was improved from the coupled model. The typhoon track errors after 36-h decreased due to the improvement of steering flow on the west side of subtropical high from the coupled model. However, the difference of typhoon intensity errors was insignificant, which might mean that the differences of forecasted  $T_s$  and heat flux between uncoupled and coupled model are small. The reasons for the small difference need to be further investigated.



**Citation:** Zhang, Y.; Xu, D.; Chen, Z.; Meng, W. Offline Diagnostics of Skin Sea Surface Temperature from a Prognostic Scheme and Its Application in Typhoon Forecasting Using the CMA-TRAMS Model over South China. *Atmosphere* **2022**, *13*, 1324. <https://doi.org/10.3390/atmos13081324>

Academic Editors:  
Anastasios Papadopoulos and  
George Varlas

Received: 2 June 2022

Accepted: 15 August 2022

Published: 19 August 2022

**Publisher's Note:** MDPI stays neutral with regard to jurisdictional claims in published maps and institutional affiliations.



**Copyright:** © 2022 by the authors. Licensee MDPI, Basel, Switzerland. This article is an open access article distributed under the terms and conditions of the Creative Commons Attribution (CC BY) license (<https://creativecommons.org/licenses/by/4.0/>).

**Keywords:**  $T_s$  prognostic scheme; offline diagnostics; CMA-TRAMS model; typhoon; track error

## 1. Introduction

The surface type of the numerical model can be classified into two categories: land and ocean. The exchange of matter and energy between the atmosphere and land or between the atmosphere and ocean directly determines the latent flux, sensible heat flux, and momentum flux at the bottom layer of the model. These fluxes all have a significant impact on the development of the model boundary layer and related physical processes. The physical mechanisms of the atmosphere and land or atmosphere and ocean interactions are considerably different, and different parameterization schemes must be designed to describe them.

The influence of the ocean on the atmosphere mainly occurs via the transport of heat and water vapor to the atmosphere. The transport rate mainly depends on the ocean surface temperature and the vertical distribution of wind, temperature, and humidity in the atmospheric boundary layer. The nonlinear interactions between them have a significant impact on the occurrence and development of small- and medium-scale convective systems. Cold water integrates into the mixed layer through physical processes such as entrainment and suction via the convection system, which reduces the sea surface temperature (SST).

In contrast, the latent and sensible heat fluxes decrease and the intensity of the convective system weakens owing to a reduction in the SST. Therefore, the SST is a key variable driving air–sea interactions. Traditionally, the SST is referred to as the bulk SST, which refers to the mean temperature of the top ocean layer of about 10 m in depth [1,2]. This value should be the actual interfacial temperature between the ocean and air, i.e., skin sea surface temperature ( $T_s$ ). The diurnal variability in the  $T_s$  has a direct influence on the surface fluxes and atmospheric variability from diurnal to intraseasonal time-scales [3,4]. However, there exist some uncertainties of estimating the  $T_s$  using satellite. Llewellyn-Jones [5] pointed out that the accuracy with which  $T_s$  could be measured using satellite infrared radiometers was limited primarily by uncertainties in the correction for atmospheric effects upon the measured  $T_s$ . Murray et al. [6] compared the difference of the  $T_s$  measured by the Along Track Scanning Radiometer (ATSR) with bulk temperature from moored buoy array and found that ATSR provided the first remotely-sensed  $T_s$  at the accuracy required to conduct a study of the skin-bulk effect. In addition, inevitably considerable noise about ATSR was also considered. Al-Shehhi [7] indicated that remotely sensed  $T_s$  might reveal uncertainties due to factors such as water depth and turbidity.

Consequently, many methods can be used for diagnosing the  $T_s$ . Fairall et al. [1] first developed separate models for the cooling skin and the warm layer effects. Within a few millimeters of the uppermost ocean layer, a net cooling of the subsurface associated with molecular motion produces a cold surface layer. During the day, a warm layer appears at a depth of several meters owing to the absorption of incoming shortwave radiation. Based on this diagnostic model, they found that the difference in the net surface heat flux, as calculated based on the  $T_s$  and bulk SST, was 11 W/m<sup>2</sup>. Clayson et al. [8] and Gentemann et al. [9] developed empirical formulas to estimate the diurnal  $T_s$  based on wind and solar insolation. Zeng et al. [10] derived a theoretical relationship to estimate the diurnal  $T_s$  using wind speed and the diurnal variation in the bulk SST, as measured by buoys. However, these approaches are less suitable for numerical model simulation because they are not rigorous enough, utilize a fixed diurnal cycle in  $T_s$ , or need the diurnal cycle of bulk temperature as input. In an attempt to develop a  $T_s$  prognostic scheme, Beljaars [11] reformulated the diagnostic relationships proposed in Webster et al. [4] as a prognostic equation for the  $T_s$ . Zeng and Beljaars [12] developed a new prognostic scheme for the  $T_s$ . This scheme implemented rigorously derived equations for the cool skin and warm layer effects, which produced realistic diurnal cycles when using observed surface fluxes in both tropical and mid-latitude locations. When preliminarily implemented into a three-member ensemble in the European Centre for Medium-Range Weather Forecasts (ECMWF) model, this scheme yielded changes in the average annual latent heat flux in excess of 10 W/m<sup>2</sup> in some oceanic regions. Brunke et al. [13] applied the scheme proposed in Zeng et al. [12] to the Community Atmosphere Model (CAM3.1) and found that the diurnal cycles in air temperature and precipitation had been substantially influenced over regions with large  $T_s$  diurnal cycles. Particularly, the hourly maximum precipitation rates in the Bay of Bengal and Western Pacific increase during the summer monsoon. Takaya et al. [14] improved a Monin–Obukhov similarity function for stable conditions and mixing enhancement based on Langmuir circulation of the warming layer using the scheme proposed in Zeng et al. [12]. The modified scheme was characterized by better agreement between the diurnal  $T_s$  amplitude and that from satellite observations. Furthermore, they found that the parameterization of the Langmuir circulation effect enhanced ocean mixing and reduced diurnal variability in the  $T_s$  under big waves conditions.

Additionally, many studies have implemented coupled atmosphere-ocean forecasting models by employing more accurate simulations of how the ocean impacts the atmosphere at shorter time-scales [15–17]. More and more coupled atmosphere–ocean models are applied to operational numerical weather predictions [18–21]. Further, some studies have discussed the influence of air-sea interactions on severe weather systems using coupled atmosphere-ocean models [22–25]. Schade et al. [26] coupled the axisymmetric typhoon model with the three-layer ocean–atmosphere model and found that the sea surface cooling

caused by typhoons could weaken the typhoon's intensity by >50%. Jiang et al. [27] coupled the MM5 mesoscale model with the POM regional ocean model and found that this coupled scheme could effectively improve the forecast effects of the Krovanh typhoon. Wu et al. [28] found that the coupled WRF-ROMS model indicated high simulation accuracy with respect of storm surge in the South China Sea under the influence of Typhoon Kai-tak. The heat exchange at the air-sea interface was very strong under the influence of Typhoon Kai-tak, and the latent heat generated by water vapor evaporation plays a dominant role in the heat exchange at the atmosphere and ocean interface. Zhao et al. [29] found that the coupled WRF-ROMS model could well simulate TC intensity changes and SST cooling induced by the TCs under different ocean MLD and background flow conditions. Heo et al. [30] simulated binary typhoons based on the coupled model of WRF and WAM and found a large surface temperature cooling caused by vertical mixing and upwelling induced by the previous typhoon resulted in a significant decrease in intensity and change in the movement speed of the net typhoon. Sun et al. [31] indicated that the simulated TC was weakening using coupled model because lower SST and increased surface roughness of the sea waves caused by the TC. Lim et al. [32] these intricate interactions between atmosphere and ocean required a fully coupled Weather Research and Forecasting (WRF)-ROMS-SWAN model to best reproduce the environment during a typhoon.

Previous studies had reported that atmosphere and ocean coupled model could well simulate TC intensity and SST cooling; therefore, the coupled scheme could effectively improve the forecast effects of typhoon. However, the coupled model is quite complex and the choice of the coupler is a key to couple air-ocean model. In addition, the computational cost is much higher with the coupled model and operational forecasting is hard to guarantee within limited computer resource. The  $T_s$  prognostic scheme is relatively simple and easier to couple with atmospheric model. Furthermore, there are lower computer cost and high calculating efficiency using the model after coupling  $T_s$  scheme. Comparing the advantages and disadvantages between the air-ocean coupled model and  $T_s$  scheme coupled atmospheric model as well as operational application, the latter could be a better choice at the present stage.

Now, the  $T_s$  used in the Tropical Regional Atmospheric Model System of South China of the China Meteorological Administration (CMA-TRAMS) is assumed to be fixed in the forecasting process. The scheme proposed by Zeng et al. [12] was introduced into the operational version of the ECMWF model from 2008 to the present [33]. In order to consider the atmosphere and ocean interaction in the numerical weather prediction model of South China, we implement this scheme into the CMA-TRAMS and investigated its impact on the predictable variables, including temperature, specific humidity and wind speed as well as typhoon predictions. In this paper, Section 2 describes the  $T_s$  prognostic scheme. Section 3 diagnoses the offline effect of the  $T_s$  prognostic scheme based on observations from BoHe Base over South China. Section 4 evaluates and discusses the impact of the  $T_s$  prognostic scheme on the simulated temperature, humidity and wind speed as well as typhoons in CMA-TRAMS. Finally, Section 5 summarizes and interprets our results.

## 2. Description of $T_s$ Prognostic Scheme and CMA-TRAMS Model

### 2.1. $T_s$ Prognostic Scheme

The one-dimensional heat transfer in the ocean can be written as the molecular thermal conductivity:

$$\frac{\partial T}{\partial t} = \frac{\partial}{\partial z}(K_w + k_w) \frac{\partial T}{\partial z} + \frac{1}{\rho_w c_w} \frac{\partial R}{\partial z}, \quad (1)$$

where subscript w refers to sea water,  $T$  is the sea water temperature, and  $z$  is the depth (up is defined as the positive direction),  $\rho_w$  and  $c_w$  are the density and volumetric heat capacity of sea water, respectively,  $K_w$  and  $k_w$  are the turbulent diffusion coefficient and the molecular thermal conductivity of water, respectively, and  $R$  is the net solar radiation flux (up is defined as the positive direction).

In the oceanic molecular sublayer at a depth of  $\delta$ ,  $K_w$ , and  $\frac{\partial T}{\partial t}$  are assumed to be negligible; therefore Equation (1) can be rewritten as follows:

$$\frac{\partial}{\partial z} \left( k_w \frac{\partial T}{\partial z} \right) = - \frac{1}{\rho_w c_w} \frac{\partial R}{\partial z}. \quad (2)$$

The upper boundary condition ( $z = 0$ ) is assumed as follows:

$$k_w \rho_w c_w \frac{\partial T}{\partial z} = Q = LH + SH + LW, \quad (3)$$

where  $LH$ ,  $SH$ , and  $LW$  indicate the latent heat flux, sensible heat flux, and net long-wave radiation, respectively, defined as positive downward. The integration of Equation (2) yields the following:

$$\rho_w c_w k_w \frac{\partial T}{\partial z} = Q + R_s - R(z). \quad (4)$$

Further integration of Equation (4) yields the following:

$$T_s - T_{-\delta} = \frac{\sigma}{\rho_w c_w k_w} (Q + R_s f_s), \quad (5)$$

where  $R_s$  is the net solar radiation near the sea surface and  $f_s$  is the fraction of solar radiation absorbed in the sublayer [1,12,34].

$$f_s = 0.065 + 11\delta - \frac{6.6 \times 10^{-5}}{\delta} \left[ 1 - \exp \left( -\frac{\delta}{8 \times 10^{-4}} \right) \right]. \quad (6)$$

The thickness of the skin layer ( $\delta$ ) is obtained from Fairall et al. (1996):

$$\delta = 6 \times \left[ 1 + \left( \frac{-16g\alpha_w v_w^3}{u_* w^4 k_w^2 \rho_w c_w} Q + R_s f_s \right)^{3/4} \right]^{-1/3}, \quad (7)$$

where  $\alpha_w$  ( $= \max(10^{-5}, 10^{-5}(T_{-d} - 273))$ ) is the thermal expansion coefficient of water and  $v_w$  ( $= 1.7558 \times 10^{-6} - 5.1029 \times 10^{-6} \times (T_{-\delta} - T_0) + 6.4864 \times 10^{-10} \times (T_{-\delta} - T_0)^2$  ( $m^2 s^{-1}$ )) is the kinematic viscosity,  $u_* w$  ( $= u_* a \sqrt{\frac{\rho}{\rho_w}}$ ) is the friction velocity in sea water,  $\rho_w$  ( $= 1025 \text{ kg m}^{-3}$ ) is the density at the skin surface of sea water,  $c_w$  ( $= 4190 \text{ J kg}^{-1} K^{-1}$ ) is the volumetric heat capacity of sea water, and  $k_w$  ( $= 1.4 \times 10^{-7} \text{ W m}^{-1} K^{-1}$ ) is the molecular thermal conductivity of sea water.

Within a depth of  $d$  below the skin sea surface (i.e., the measurement depth at which the diurnal cycle can be omitted), the effect of  $k_w$  is not as pronounced as that of  $K_w$ , where  $k_w$  is ignored and  $K_w$  was calculated as follows [35]:

$$K_w(z) = \frac{k u_* w (-z)}{\phi_t \left( \frac{-z}{L} \right)}, \quad (8)$$

where  $k = 0.4$ , i.e., the Von Karman constant. When  $d \gg \delta$ , we assume that  $T = T_{-\delta} - [(z + \delta)/(-d + \delta)]$ . Integrating Equation (1) based on Equations (4) and (8), we obtain Equation (9) as follows:

$$\frac{\partial}{\partial t} (T_{-\delta} - T_{-d}) = \frac{Q + R_s - R(-d)}{d \rho_w c_w v / (v + 1)} - \frac{(v + 1) k u_* w}{d \phi_t (d/L)} (T_{-\delta} - T_{-d}), \quad (9)$$

where the stability function is as follows:

$$\phi_t \left( \frac{-z}{L} \right) = \begin{cases} 1 + 5 \frac{-z}{L}, & \text{for } \frac{-z}{L} \geq 0 \\ (1 - 16 \frac{-z}{L})^{-1/2}, & \text{for } \frac{-z}{L} < 0. \end{cases} \quad (10)$$

The Monin–Obukhov length is calculated as follows:

$$L = \frac{\rho_w c_w u_{*w}^3}{k F_d}. \quad (11)$$

The buoyancy flux is calculated as follows:

$$F_d = g\alpha_w [Q + R_s - R(-d)] \quad \text{for } (T_{-\delta} - T_{-d}) \leq 0 \quad (12)$$

$$F_d = \left(\frac{v g a_w}{5d}\right)^{1/2} \rho_w c_w u_{*w}^2 (T_{-\delta} - T_{-d})^{1/2} \quad \text{for } (T_{-\delta} - T_{-d}) > 0. \quad (13)$$

The solar radiation at depth  $d$  is:

$$R(-d) = R_s \sum_{i=1}^3 a_i e^{-db_i}, \quad (14)$$

where  $(a_1, a_2, a_3) = (0.28, 0.27, 0.45)$ ,  $(b_1, b_2, b_3) = (71.5, 2.8, 0.06m^{-1})$ . The profile shape parameter,  $\nu$ , is the empirical parameter in Equation (9), which is set to 1.0 in Fairall et al. [1] and 0.3 in Zeng et al. [12].

The cooling temperature of the cool ocean skin ( $T_s - T_{-\delta}$ , i.e.,  $\Delta T_c$ ) and warming temperature of the warm layer ( $T_{-\delta} - T_{-d}$ , i.e.,  $\Delta T_w$ ) are obtained based on Equations (5) and (9), respectively. The forecasting is calculated using the initial temperature ( $T_b$ ) overlaying the above temperatures. Here, is calculated as follows:

$$T_s = T_b + \Delta T_c + \Delta T_w. \quad (15)$$

## 2.2. CMA-TRAMS Model

CMA-TRAMS is based on the Global/regional assimilation and prediction system (GRAPES) non-hydrostatic mesoscale model. The semi-implicit-semi-Lagrangian time difference scheme is applied in this model. The model has a longitude–latitude grid, the Arakawa-C grid leapfrog scheme, and the Charney–Philips vertical layering scheme. The vertical coordinate of the model is the height terrain-following coordinate. A series of technical solutions for model dynamical frame have been implemented based on the original GRAPES model. For example, the three-dimension reference profile has replaced the one-dimension reference profile. More recent studies have improved the step-by-step calculation method for the nonlinear term in the semi-implicit-semi-Lagrangian time difference scheme and the coupling technology between the dynamical and physical processes [36]. At present, the physical schemes of this model include RRTMG long and short wave radiation, Weather Research and Forecasting (WRF) Single-Moment 6-class (WSM6) microphysical, improved New Simplified Arakawa-Shubert (NSAS) convective parameterization scheme [37], Simplify Model for land Surface (SMS) parameterization scheme with forecasts of the soil moisture in the shallow soil layer [38], New Medium Range Forecast (NMRF) boundary layer parameterization scheme [39], and gravity wave drag induced by the sub-grid orograph parameterization scheme [40]. Furthermore, the physical process considers the coupling between the convective parameterization scheme and the microphysical scheme is considered [41]. The revised near-surface heat flux formula in this model could improve the forecast of typhoon track and intensity [42]. The model used in this study ranged from  $70^\circ$  E to  $160^\circ$  E in the meridional zone and from  $0.8^\circ$  N to  $54.8^\circ$  N in the zonal zone (Figure 1). The horizontal grid size was  $0.09^\circ \times 0.09^\circ$  and there are 65 vertical layers in this model. The integration time step in this model is 90 s.

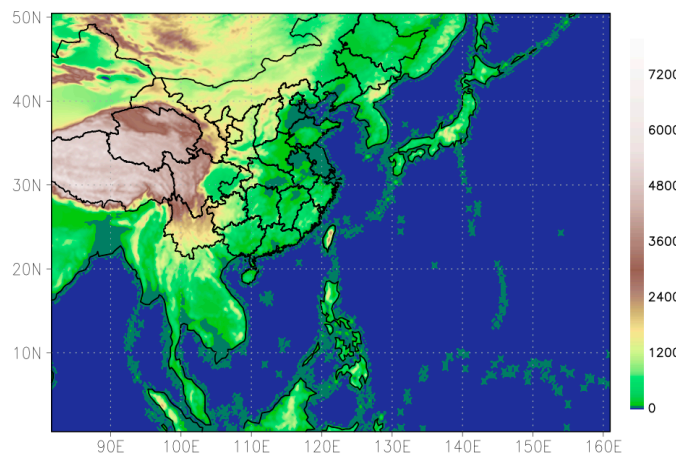


**Figure 1.** The range of CMA-TRAMS operational model over South China.

### 3. $T_s$ Prognostic Scheme Offline Diagnosis

#### 3.1. Observation Data

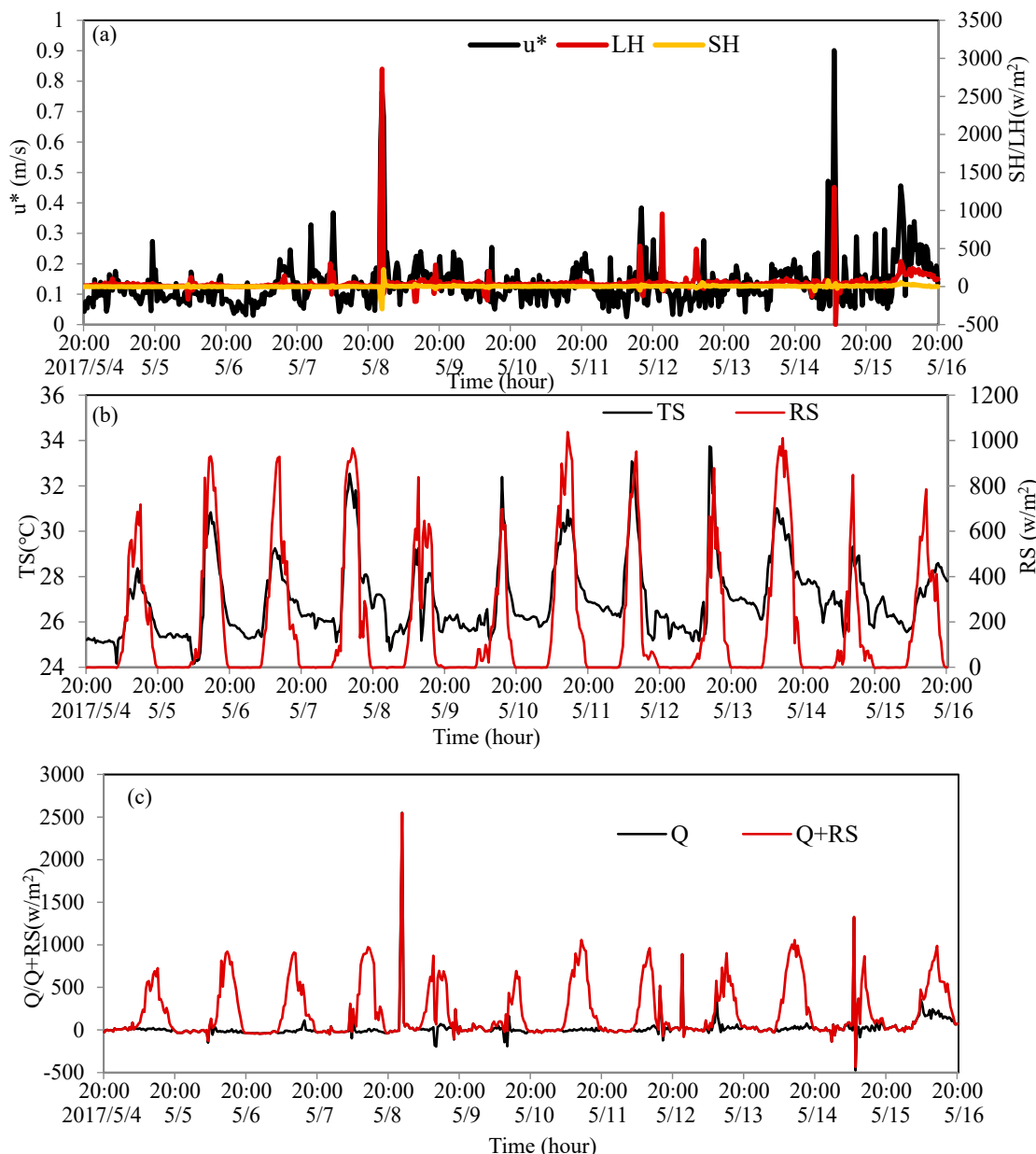
The observation datasets selected for the offline test of the  $T_s$  prognostic scheme range from 20:00 on 4 May 2017, to 20:00 on 16 May 2017 (local time, the same below), thus providing a relatively complete observation dataset from the Bohe Marine Meteorological Science Experiment Base [43]. The datasets contain 577 observations (equivalent to 12 days) at a frequency of once per half hour. The datasets include the initial  $T_s$ , net long-wave radiation (RL), net short wave radiation (RS), sensible heat flux (SH), latent heat flux (LH), friction velocity ( $u^*$ ), and  $T_s$  during the study period. The flux and friction velocity are detected at the height of 31.3 m. Huang et al. [44] had provided further details on the datasets.

Figure 2 shows the evolution of observation datasets during the study period. There is a negligible change in the amplitude of the SH, except for specific individual cases (e.g., 00:00, 00:30, and 01:00 on 9 May 2017). The amplitude of the three times exceeded  $100 \text{ W/m}^2$ , where the maximum value is  $293 \text{ W/m}^2$  and those of the other times are within  $100 \text{ W/m}^2$  (orange line in Figure 2a). The amplitude of LH varies significantly. The maximum amplitude reaches  $2857 \text{ W/m}^2$  (00:30 on 9 May 2017) while the amplitudes at other times are all within  $1500 \text{ W/m}^2$  (red line in Figure 2a). The tendency of the amplitude for  $u^*$  is identical to that of LH with time. The first and second maximum values appear at 00:30 on 9 May and 9:00 on 15 May respectively. The amplitude of  $u^*$  is approximately between 0 and 1.0 (black line in Figure 2a). The time-varying trend for the  $T_s$  is basically consistent with that of the RS. The RS has a maximum value at noon (red line in Figure 2b), and the  $T_s$  also has a maximum at the same time (black line in Figure 2b). The RS at night is zero and the  $T_s$  also has a low value. The maximum value of Q and the sum of Q and RS, as recorded at Bohe Base over 12 days, is approximately  $2500 \text{ W/m}^2$  (00:30 on 9 May 2017) and the amplitude of Q + RS (red line in Figure 2c) is below  $1500 \text{ W/m}^2$  during the other periods owing to the effect of the LH. Based on the evolution of several variables during the study period, the observed datasets are reasonable.

#### 3.2. Offline Diagnostic Results

The offline prognostic scheme for the  $T_s$  is integrated from 20:00 on 4 May 2017, to 20:00 on 16 May 2017, with a time step of 1800 s. The forcing field includes the RL, RS, SH flux, LH flux,  $u^*$ , and  $T_s$ . The  $T_s$  is used to drive the initial time of the offline scheme, as well as to verify the forecasting  $T_s$ . The profile shape parameter  $\nu$  in Equation (9) is an empirical parameter that is set to 1.0 in Fairall et al. [1] when  $\Delta T_w$  is approximately 3 K. However, Zeng et al. [12] pointed out that  $\nu$  was <1.0 under strong radiation heating. Based on 10 days of observation in the Western Pacific Warm Pool, they found that  $\nu$  was 0.3 under weak wind at approximately 3 K  $\Delta T_w$  when the peak of the surface solar radiation reached approximately  $1000 \text{ W/m}^2$  at local time. Therefore,  $\nu$  has uncertainty under

different conditions. As the 12-day peak in the surface solar radiation at Bohe base exceeds  $1000 \text{ W/m}^2$ ,  $v$  should be selected for sensitivity experiments. Generally, there is negligible diurnal variation in the SST at depths of 2–4 m, which is set to 3 m in Zeng et al. [12]. As our observation point was inshore, we also conduct a sensitivity test on the depth  $d$  of the warm layer to discuss whether the inshore  $T_s$  is sensitive to it. Usually, the  $T_b$  is determined from our subsurface in situ temperature measurements (at certain reference depth) [1], namely bulk temperature. However, such temperature does not exist in the observation datasets from the BoHe base. Therefore, the  $T_b$  is replaced by the  $T_s$  at initial moment, or the monthly averaged  $T_s$ , or  $T_s$  with the diurnal variation from the observation to investigate whether the forecasted  $T_s$  is sensitive to the  $T_b$ .



**Figure 2.** Changes in the observation datasets with time at BoHe Base: (a)  $u^*$  (black line), LH (red line), and SH (orange line); (b)  $T_s$  (black line) and RS (red line); and (c) Q (SH + LH + RL) (black line) and Q + RS (red line).

Three sets of trials (including seven total sub-experiments) were designed, as listed in Table 1. The sensitivity experiments of  $v$  are ts-v0.1-d3.0, ts-v0.2-d3.0, and ts-v0.3-d3.0,

respectively. The experiments of  $T_b$  are tsd-v0.2-d3.0 and tsm-v0.2-d3.0, respectively. The experiments of  $d$  are tsm-v0.2-d2.5 and tsm-v0.2-d3.5, respectively. Figure 3a (including three sub-experiments) shows the time-dependent changes in  $\Delta T_w$  in the first set of experiments. Three sub-experiments had diurnal variations in  $\Delta T_w$ , which are basically consistent with the diurnal changes in the solar radiation. When  $v$  is set to 0.3 (ts-v0.3-d3.0), the amplitude of  $\Delta T_w$  is below 2.3 K, with a peak of 2.234 K, which is below the results reported in Fairall et al. [1] and Zeng et al. [9] (i.e.,  $\Delta T_w$  of approximately 3 K). This may be related to the magnitude of the surface solar radiation peak. When  $v$  is reduced to 0.2 (ts-v0.2-d3.0), the amplitude of  $\Delta T_w$  increased and the peak, at 3.135 K, agreed with previous studies. Furthermore, when  $v$  is reduced to 0.1 (ts-v0.1-d3.0), a large increment existed in the amplitude of  $\Delta T_w$  and the peak is above 6 K. Such a significant variation in  $\Delta T_w$  may be unbalanced in the two terms on the right-hand side of Equation (9). Therefore, considering the characteristics of the observational dataset and the variation in the amplitude of  $\Delta T_w$ , we set  $v$  to 0.2. Here,  $\Delta T_c$  has a negligible relationship with  $v$  (Figure 3b) and its amplitude varies between 0 and 1.0 K, except for individual times exceeding 1.0 K at the peak of 1.326 K.

**Table 1.** Details of the seven sensitivity experiments.

Experiment Name	Parameter Configuration	Aim of the Experiment
ts-v0.1-d3.0	$v = 0.1$	To confirm the correct $v$ according to the amplitude of $\Delta T_w$ , where $T_b$ is $T_s$ at initial moment and $d = 3$ m (Figure 2).
ts-v0.2-d3.0	$v = 0.2$	
ts-v0.3-d3.0	$v = 0.3$	
tsd-v0.2-d3.0	$T_b = \text{tsd}$	To confirm correct $T_b$ according to the contrast between the forecasted $T_s$ and observed $T_s$ , where $v$ is the result of the first set of trials, $d = 3$ m and $T_b$ is $T_s$ with diurnal variation (tsd) and monthly averaged $T_s$ (tsm), respectively (Figure 3).
tsm-v0.2-d3.0	$T_b = \text{tsm}$	
tsm-v0.2-d2.5	$d = 2.5$ m	To confirm correct $d$ according to the contrast between the forecasted $T_s$ and observed $T_s$ , where $v$ and $T_b$ are the result of the above two sets of trials and $d = 3$ m (Figure 4).
tsm-v0.2-d3.5	$d = 3.5$ m	

Using  $v = 0.2$  and  $d = 3$  m, the second set of experiments is performed to test the sensitivity of  $T_b$  based on three settings: (1) use the initial  $T_s$  as  $T_b$ , i.e., experiment ts-v0.2-d3.0; (2) introduce the daily variation in  $T_s$  into  $T_b$ , i.e.,  $T_b$  has a daily variation in the 12-day forecasting process, which is a function of the number of days (experiment tsd-v0.2-d3.0); and (3) the monthly average  $T_s$  as  $T_b$ , i.e., experiment tsm-v0.2-d3.0.

The  $T_b$  sensitivity experiments (Figure 4) shows that the simulated  $T_s$  reflects the diurnal variation and the peak in the diurnal variation has a hysteresis similar to the findings reported in Zeng et al. [9]. When  $T_b$  is equal to the  $T_s$  at the initial moment (ts-v0.2-d3.0), the trend in the simulated  $T_s$  over the first two days is more consistent with the observation. The peak during the day is slightly smaller, whereas that during the night is similar to the observation. However, after two days, the simulated  $T_s$  is lower than the observation, with a deviation of approximately  $-2$  K at night and an ever more notable value during the day (up to  $\sim 7-8$  K). After considering the diurnal variation in  $T_b$  (tsd-v0.2-d3.0), the simulated  $T_s$  is generally higher than that in the ts-v0.2-d3.0 experiment. The peak during the day is closer to the observation, whereas the temperature at night is higher. When  $T_b$  is set as the monthly average  $T_s$  (tsm-v0.2-d3.0), the simulated  $T_s$  is between the tsd-v0.2-d3.0 and ts-v0.2-d3.0 experiment. In other words, the simulated  $T_s$  of tsm-v0.2-d3.0 in the day is lower than the observation while that at night is closer to the observation. Therefore, the choice of  $T_b$  is sensitive to the simulated  $T_s$  and the appropriate  $T_b$  could improve the simulation of  $T_s$ .

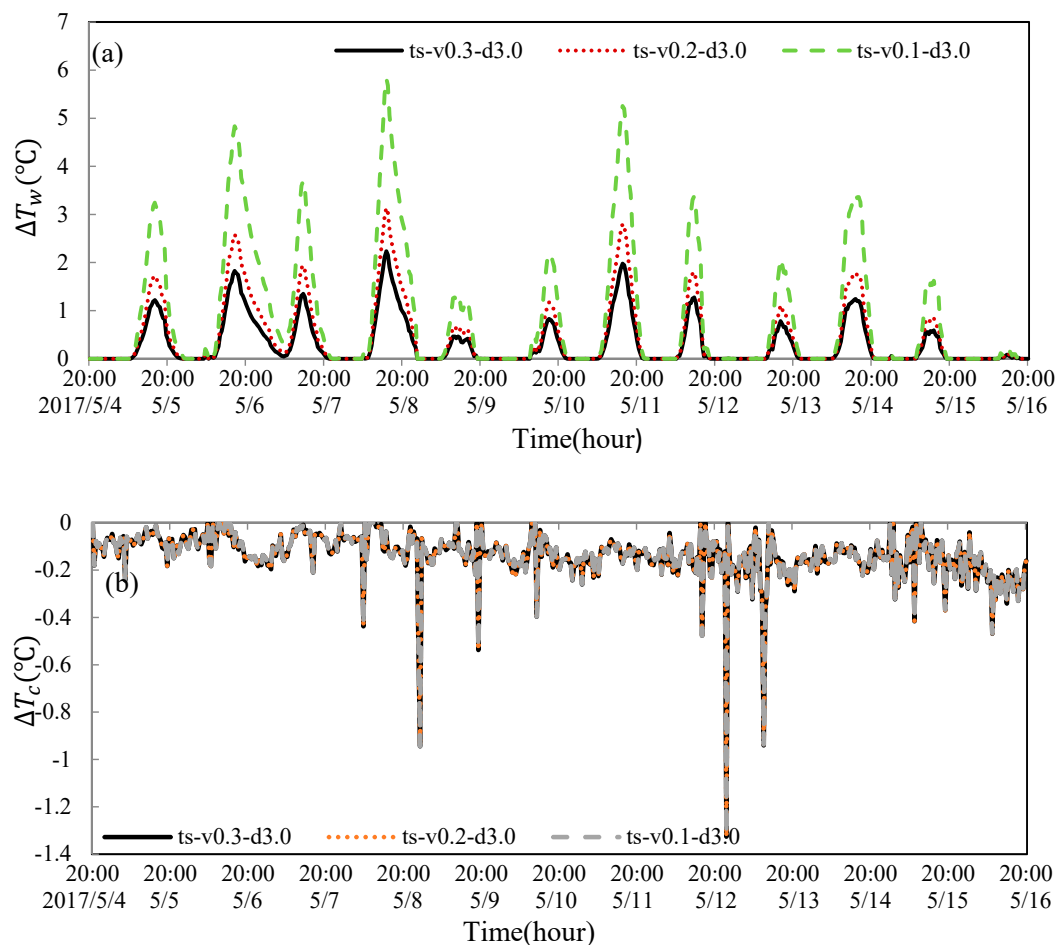


**Figure 3.** Variation in  $\Delta T_w$  (a) and  $\Delta T_c$  (b) in the first set of experiments with time (black solid line: ts-v0.3-d3.0; red-dotted line: ts-v0.2-d3.0; and green-dashed line: ts-v0.1-d3.0).

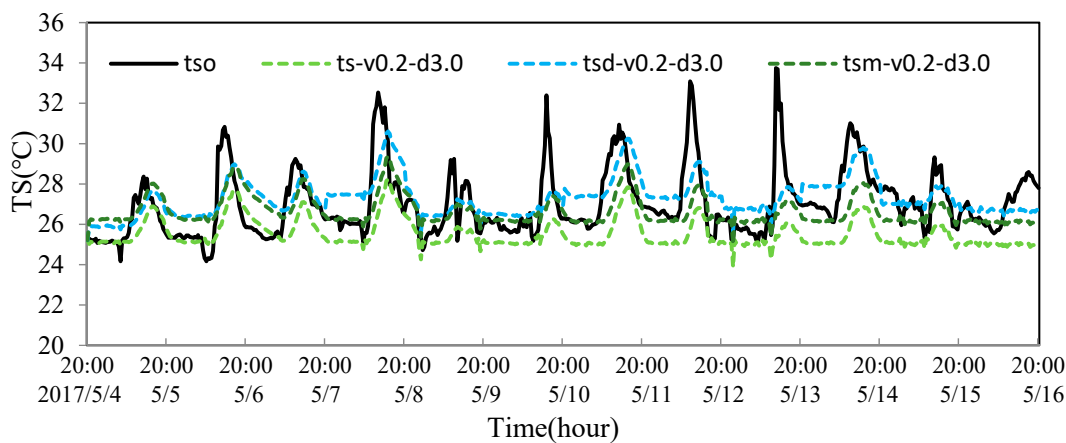


**Figure 4.** Sensitivity experiments for  $T_b$  (black bold line: observed  $T_b$  (tso); green-dashed line: ts-v0.2-d3.0; blue-dashed line: tsd-v0.2-d3.0; and dark-green-dashed line: tsm-v0.2-d3.0).

Additionally, the diurnal variation of the observed  $T_s$  is relatively large. This may be related to the fact that our observation point is inshore or that there are certain errors in the infrared observations. However, the diurnal variation in the simulated  $T_s$  was gentler than that of the observation, which may be related to the limited 3 K of the  $\Delta T_w$  in the prognostic scheme. These results should be verified using more observations, however, the observed point such as BoHe Base is scarce at present.

Based on the value of  $\nu$  and  $T_b$  from the above two experiments, the depth of the warm layer ( $d$ ) is further tested. From the curves of the simulated  $T_s$  with different  $d$  values (Figure 5a), there are no significant differences among the simulated  $T_s$ . When  $d$  is set to 2.5 m, the temperature during the day is slightly higher, while it is slightly lower at night compared to the case of  $d = 3$  m. This situation is the inverse when  $d$  is 3.5 m. Figure 5b shows the difference in the simulated  $T_s$  between  $d = 2.5$  and  $3$  m (the simulated  $T_s$  of  $d = 2.5$  m minus that of  $d = 3$  m, named Der1), as well as the difference between  $d = 3.5$  and  $3$  m (the simulated  $T_s$  of  $d = 3.5$  m minus that of  $d = 3$  m, named Der2). The amplitude of Der1 is between 0 and  $0.4$  °C with a maximum of  $0.343$  °C, where the positive value ranges from 8:00 to 17:00, and the negative value occurred after 17:00. The amplitude of Der2 is between 0 and  $0.3$  °C, but the time of the distribution from the negative and positive values is opposite that of Der1, with a slightly different corresponding time for the peak value. Therefore, based on the observations in this study, it can be concluded that  $d$  was insensitive to the simulated  $T_s$  in the offline experiments.

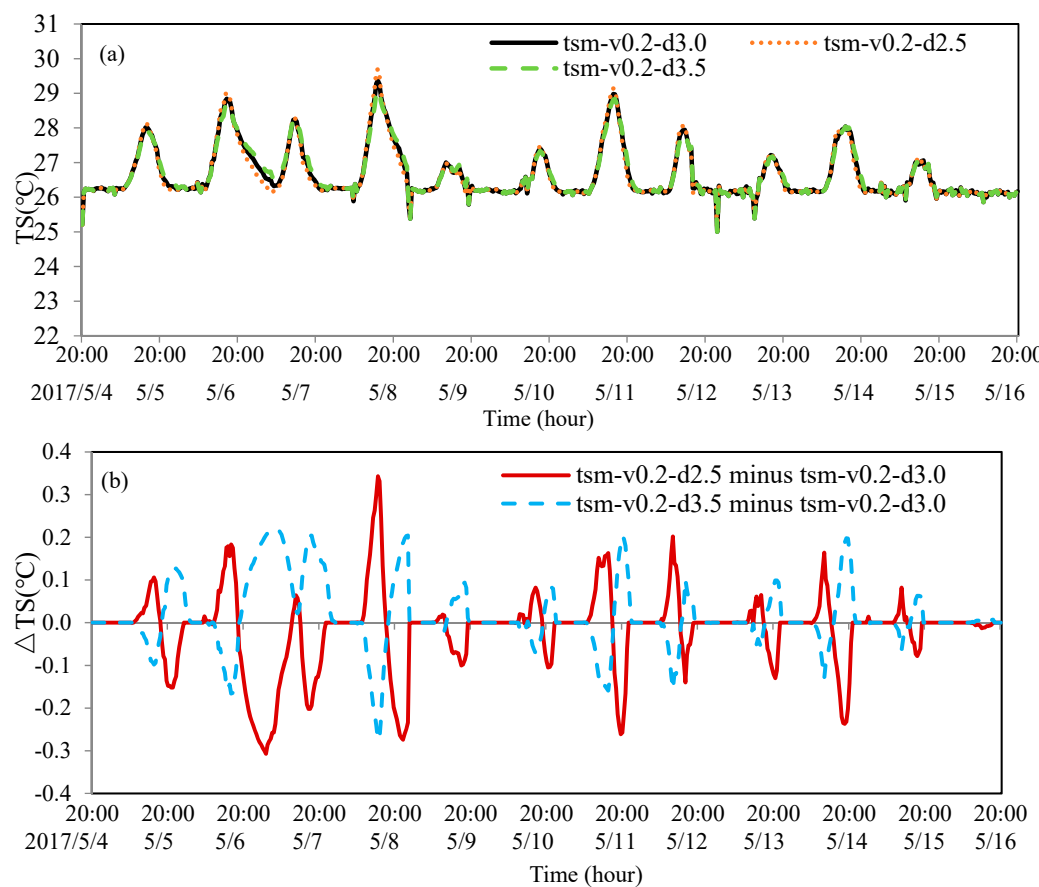


**Figure 5.** Sensitivity experiments on the warm layer depth,  $d$  (a), with variations in  $T_s$  with time (black solid line: tsm-v0.2-d3.0; red-dotted line: tsm-v0.2-d2.5; green-dashed line: tsm-v0.2-d3.5); (b) differences between the sensitivity experiments (red solid line: tsm-v0.2-d2.5 minus tsm-v0.2-d3.0; and blue-dashed line: tsm-v0.2-d3.5 minus tsm-v0.2-d3.0).

#### 4. Model Simulation

The CMA-TRAMS model without  $T_s$  prognostic scheme is named after the uncoupled model (Figure 6a), where  $T_s$  is the initial  $T_b$  and is fixed during the forecasting. The  $T_s$  prognostic scheme is coupled with the CMA-TRAMS model (Figure 6b), which is named the coupled model. The simulated effects of the coupled and uncoupled models were evaluated. All the simulations were carried out for 120-h forecasts initiated at 08:00 LST from 1–31 August 2019. Initial and lateral boundary conditions were obtained from the European Center Medium Weather Forecast (ECMWF) with a horizontal grid-size of  $0.1^\circ \times 0.1^\circ$  every

6 h. When the  $T_s$  prognostic scheme was applied to the atmospheric model,  $T_b$  was taken as the climatological SST from the study of Brunke [13] or was the bulk SST from other scholars [12,32]. Here, the inversed SST via satellite was set as  $T_b$ . The SST is the daily average dataset inversed by the combined microwave and infrared channel data. The horizontal resolution of the inversed data is  $0.0879^\circ \times 0.0879^\circ$ , with a total of  $4096 \times 2048$  points (<http://data.remss.com/> (accessed on 15 May 2022))

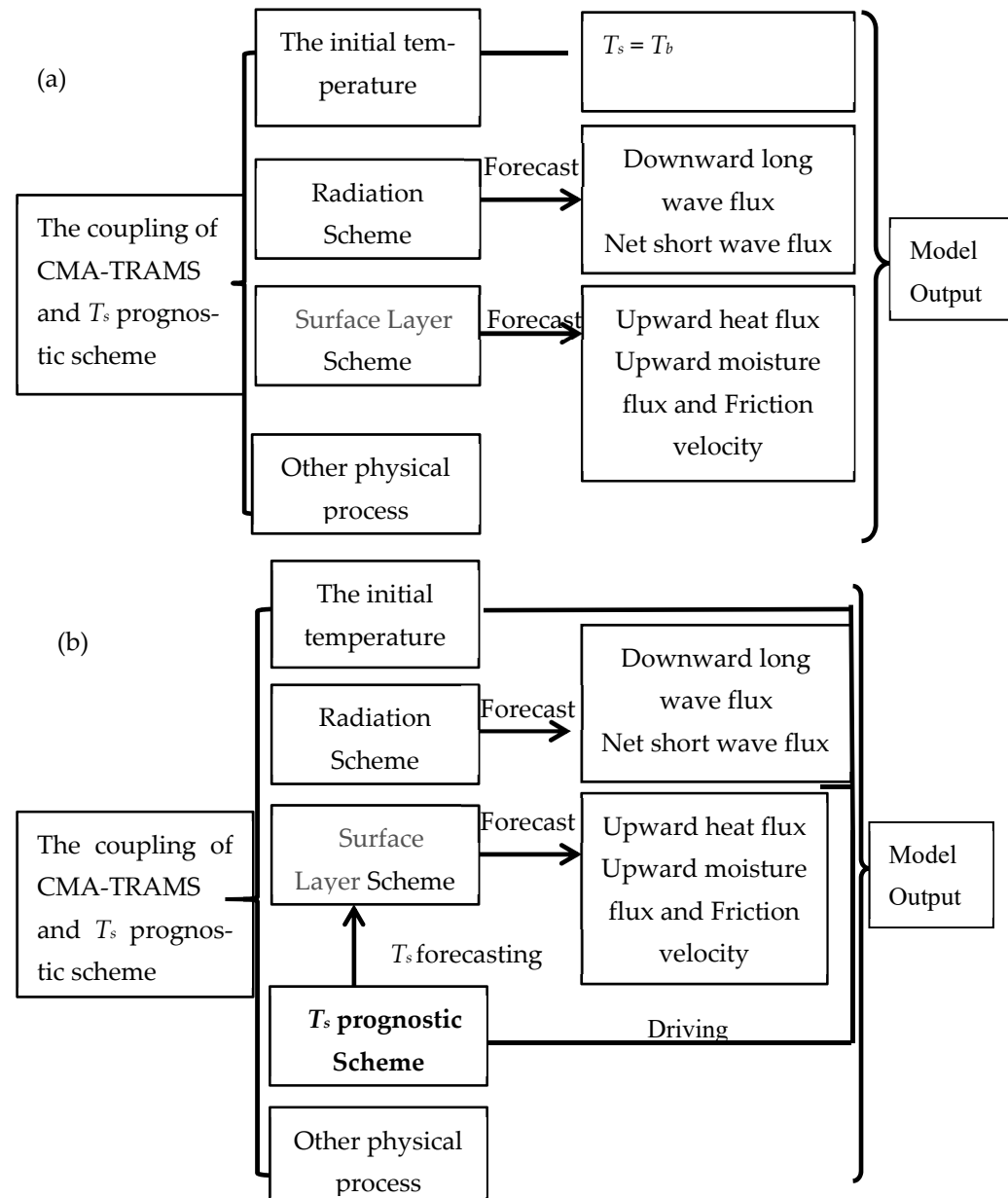


**Figure 6.** The diagram of the uncoupling (a) and coupling (b) between CMA-TRAMS and  $T_s$  prognostic scheme.

Two model experiments were designed such that the uncoupled  $T_s$  prognostic scheme is used as the control experiment (NCOU) and the coupled scheme is termed the sensitivity experiment (COU). We first evaluated the differences between the forecasted  $T_s$  in the two experiments. The bias and RMSEs of the different variables (temperature, wind speed, and specific humidity) in the two experiments were analyzed. Additionally, the forecasting effects of typhoons were investigated.

#### 4.1. Differences in $T_s$ between the Experiments

We provide a comparison of the 120-h forecasted  $T_s$  at a single point on any day from the two experiments without the observation. Figure 7 shows the 120-h forecasted  $T_s$  for 3 August 2019 at a single point ( $140^\circ$  E,  $20^\circ$  N). The results show that the simulated  $T_s$  of COU has diurnal variation. Especially during the simulation of the first 3 days, the diurnal variation is notable with the maximum temperature at noon (14:00) and minimum temperature at night (02:00). After day 3, more cloud reduces solar radiation reaching the ground due to influence of Typhoon Francisco (1908) in the West Pacific, which results in the diurnal variation decreasing. The  $T_s$  of NCOU is fixed during the simulation, which may influence the interaction between atmosphere and ocean.

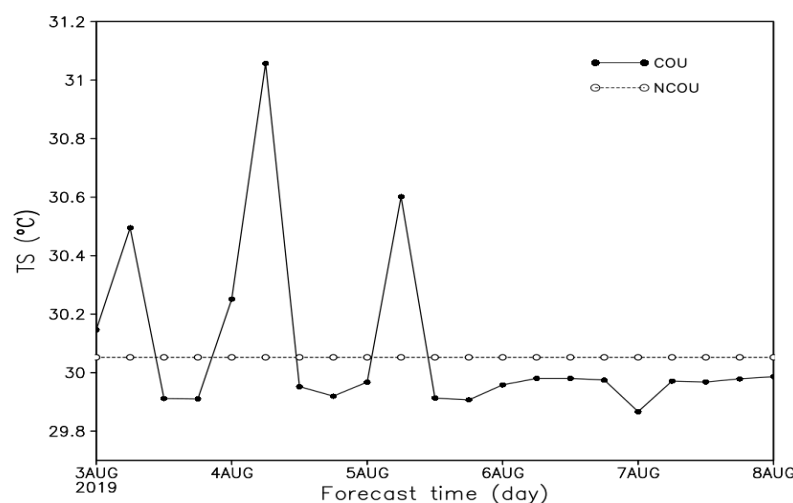


**Figure 7.** 120-h forecasted  $T_s$  at a single point ( $140^\circ$  E,  $20^\circ$  N) on 3 August 2019, in two experiments (solid line: COU; dotted line: NCOU).

Due to the observed  $T_s$ , Figure 8 shows the forecasted  $T_s$  at 24 h, 48 h, 72 h, 96 h and 120 h every day from 1 to 31 August in the COU and NCOU experiments along  $140^\circ$  E and  $20^\circ$  N. On the whole, the variation tendency of the forecasted  $T_s$  within 120 h in the two experiments are almost identical. The amplitudes of forecasted  $T_s$  from 1 to 9 August and from 18 to 31 August are relatively small. However, the forecasted  $T_s$  obviously reduces from 10 August and the amplitude is larger during 10–17 August, which is mainly affected by Typhoon Krosa (1910). Specifically, there exists a larger difference of  $T_s$  between NCOU and COU during the period influenced by typhoon, while the difference is relatively smaller when there is no obvious synoptic system. The reasons might be that the forecasted  $T_s$  has a diurnal variation after considering  $T_s$  scheme in the model while the  $T_s$  is susceptible to solar radiation. The solar radiation decreases when the cloud cover influenced by typhoon increases which induces the variation of  $T_s$ . The differences of forecasted  $T_s$  between NCOU and COU are usually within 1 K with the maximum of 1 K on August 13. These show that there exists a certain difference of  $T_s$  whether the  $T_s$  scheme is coupled with numerical model under the obvious synoptic system.

Furthermore, Figure 9 shows the regional average  $T_s$  of two experiments over the study area ( $5^\circ$  N to  $25^\circ$  N,  $130^\circ$  E to  $150^\circ$  E) at 24 h, 48 h, 72 h, 96 h and 120 h every day from August 1 to 31. There is a certain difference in the forecasted  $T_s$  of NCOU and COU from August 1 to 15, which is because that several typhoons, such as Typhoon Francisco (1908), Typhoon Lekima (1909), Typhoon Krosa (1910), occurred successively over the above region during the period. The difference of  $T_s$  is within 0.5 K. In addition, the  $T_s$  of the two experiments reduces due to the influence of typhoons from August 1 to 15. After August 16, the weather over the region is relatively stable and the difference of  $T_s$  between NCOU and COU is smaller.

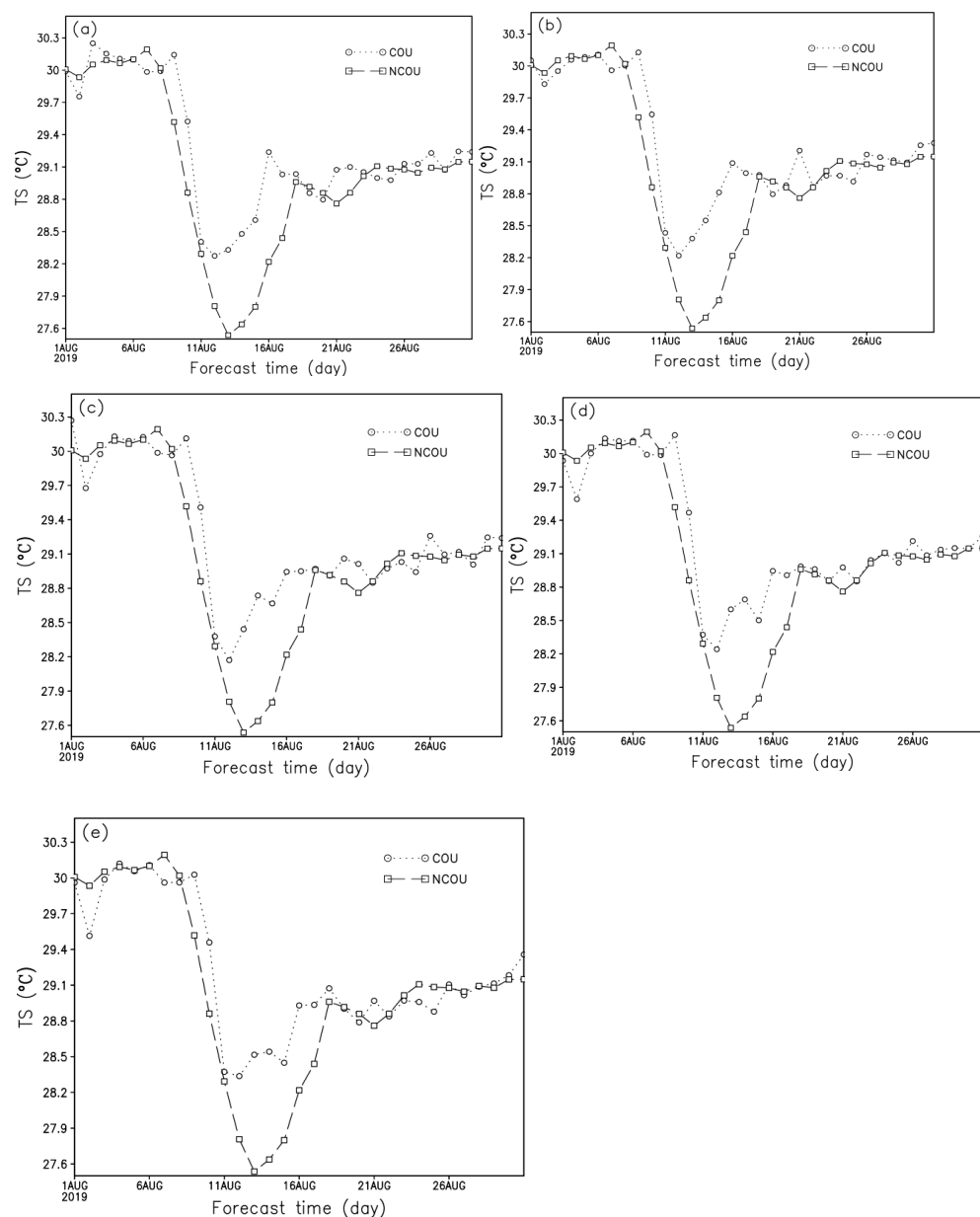


**Figure 8.** The forecasted  $T_s$  of the two experiments along  $114^\circ$  E and  $20^\circ$  N from 1 August 31 August. (a–e) respectively show the forecasts from 24 h, 48 h, 72 h, 96 h and 120 h (dotted line: COU; dashed line: NCOU).

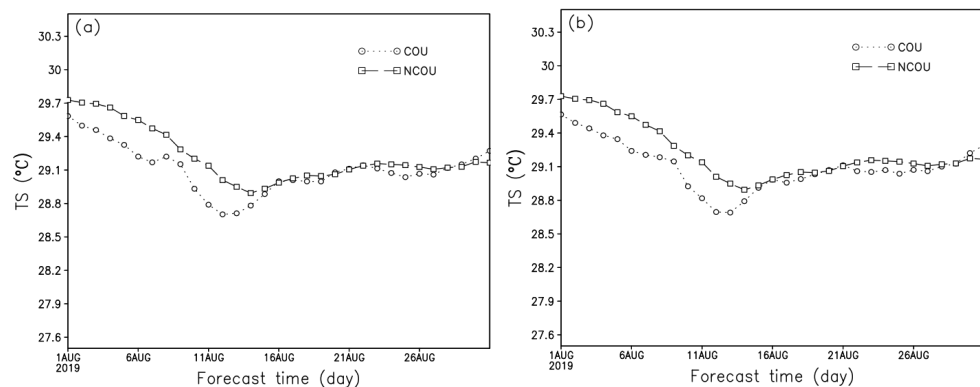


**Figure 9. Cont.**

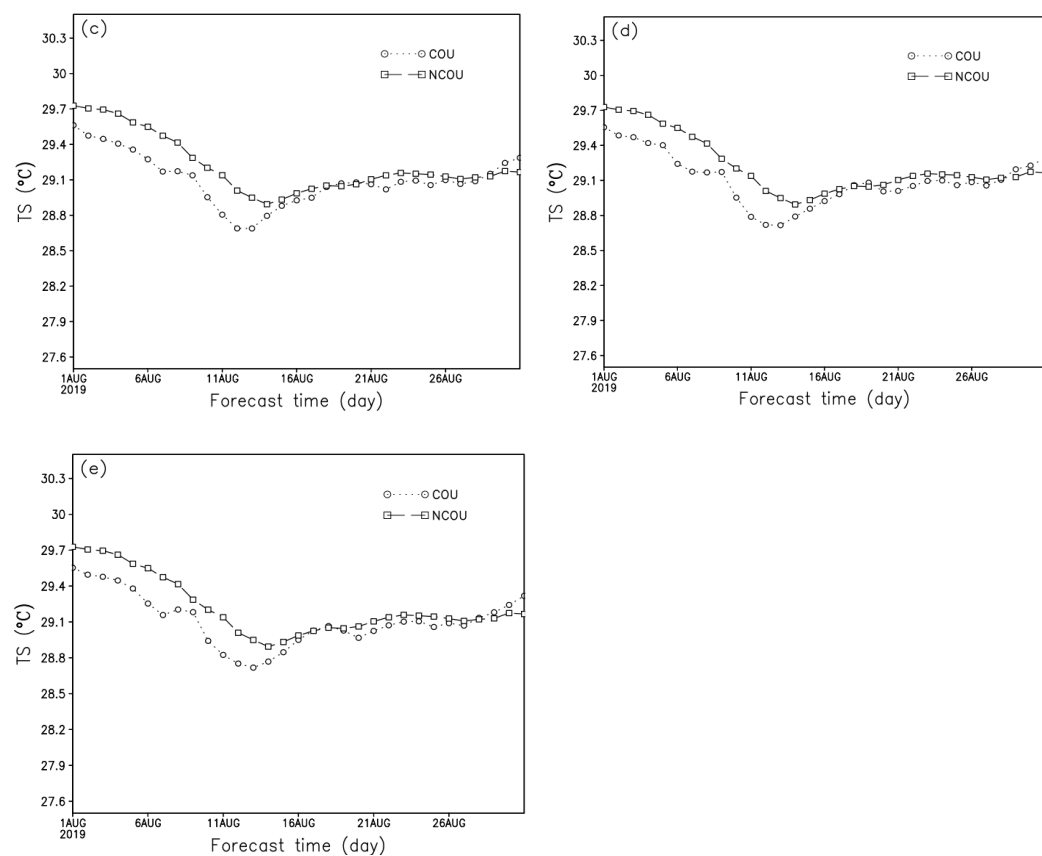


**Figure 9.** The forecasted  $T_s$  of the two experiments in the average region over  $5^\circ$  N to  $25^\circ$  N and  $130^\circ$  E to  $150^\circ$  E from 1 August 31 August. (a–e) respectively show the forecasts from 24 h, 48 h, 72 h, 96 h and 120 h (dotted line: COU; dashed line: NCOU).

#### 4.2. Impacts on Medium-Range Skill Scores

We statistically verify the  $T_s$  prognostic scheme's impacts on the medium-range forecasts against the ECMWF analysis data with a horizontal resolution of  $0.1^\circ \times 0.1^\circ$ . First, the model performance of the simulated temperature (specifically, the humidity and wind speed during August 2019) is compared with the ECMWF analysis dataset. Figure 8 depicts the time-series of the vertical profiles for the biases and RMSEs of the simulated temperature, specific humidity, and wind speed in the NCOU and their differences between the NCOU and COU (i.e., COU minus NCOU), averaged over all of the model regions, except for the boundary. The impacts of the  $T_s$  on the temperature, specific humidity, and wind speed at the middle-low level are usually prominent; therefore, the biases and RMSEs under 500 hPa are analyzed and compared between the NCOU and COU.

In the NCOU, a warm bias dominates below 950 hPa in all 5-day forecasts, with apparent increases over the forecast time. Cold biases appear above 950 hPa while the biases above 725 hPa become weaker with forecast time progression. Cold biases between 950 and 725 hPa from days 2 to 5 were slightly stronger with biases of approximately 1 K (Figure 10a). The COU experiment exerts an effect on such biases by contributing toward a decreasing warm bias below 950 hPa while increasing the cold bias above 950 hPa over the forecast time. The increasing cold bias is relatively weaker with a bias below 0.04 K. A diurnal variation in the forecasted  $T_s$  modifies the warm biases below 950 hPa in the COU. This change reduces the RMSE below 950 hPa over the forecast time (Figure 10b). The NCOU simulates a moist bias over most levels from the first to third day forecasts, except for the boundary layer in the forecast for day 3. A weak dry bias for most layers appears over the fourth- and fifth-day forecast (Figure 10c). Moist biases below 800 hPa significantly improve when considering the diurnal  $T_s$ ; the RMSEs during the forecast period decrease (Figure 10d). Furthermore, the NCOU simulates an overall positive bias in

the wind speed for most layers during the forecast time and a weak negative bias above 525 hPa (Figure 10e). The positive biases are overall significantly modified from the NCOU to the COU for most layers in the forecast, with apparent reductions in the RMSEs during the study period (Figure 10f). This suggests that changes in the temperature, moisture, and wind speed from the NCOU to the COU modulated the overall forecast accuracy in the lower atmospheric layers by decreasing the conventional biases in the temperature, moisture, and wind speed.

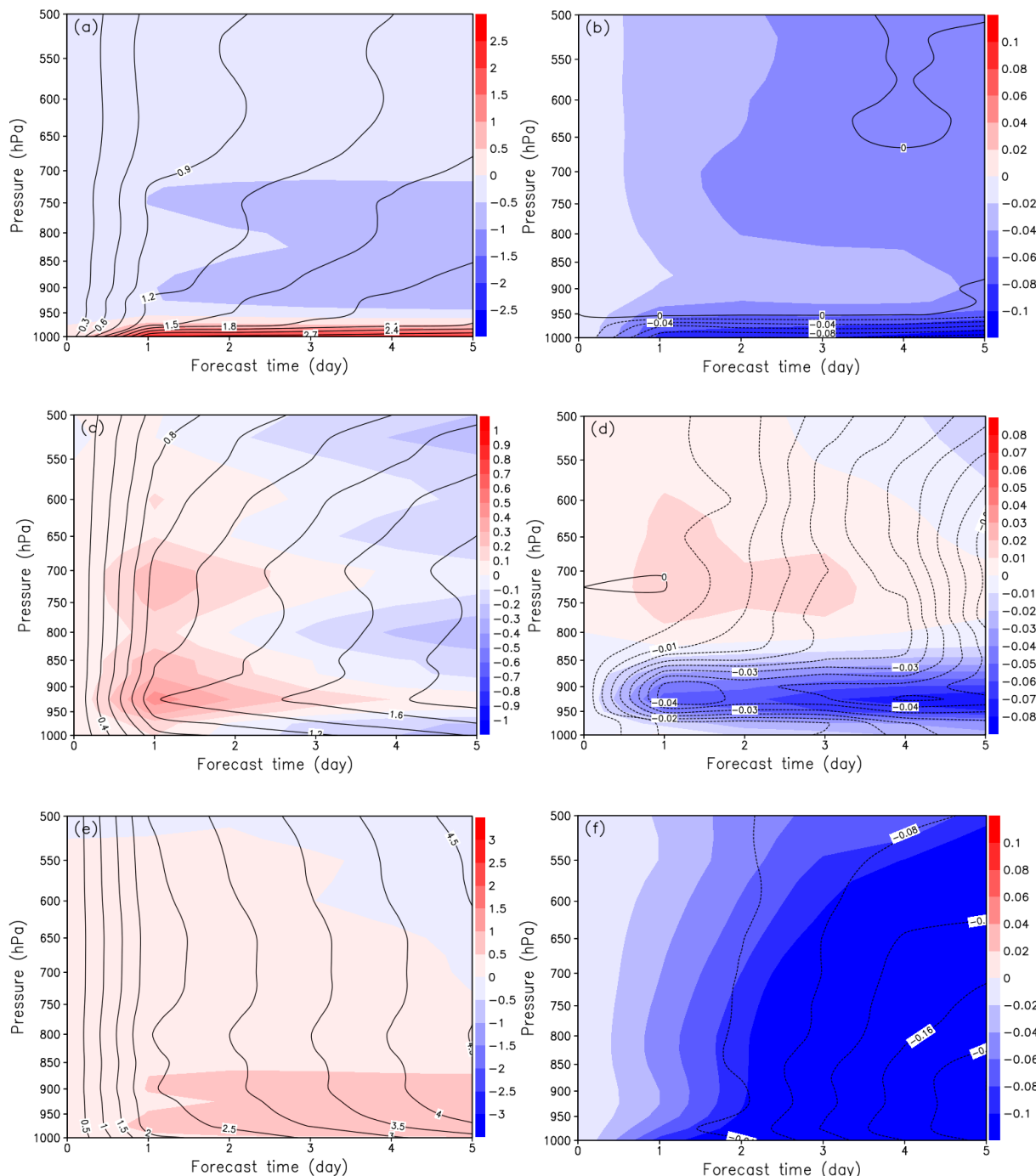


**Figure 10.** Time-pressure cross-sections of the biases (shaded) and RMSEs (contour) for the temperature (K), specific humidity ( $\text{g kg}^{-1}$ ), and wind speed ( $\text{m s}^{-1}$ ) in (a,c,e), respectively. NCOU against the EC analysis data and (b,d,f) their differences between the NCOU and COU (i.e., COU minus NCOU), averaged over the model region during August 2019. Solid and dashed lines indicate positive and negative values, respectively.

Based on these contrasts in the temperature, moisture, and wind speed between the COU and NCOU experiments, the biases and RMSEs of the temperature and moisture for the lower layers and those of the wind speed for most layers over the majority of the forecast period from the COU are reduced. This indicates that the accuracies for the atmosphere within the boundary layer are improved after coupling the  $T_s$  prognostic scheme.

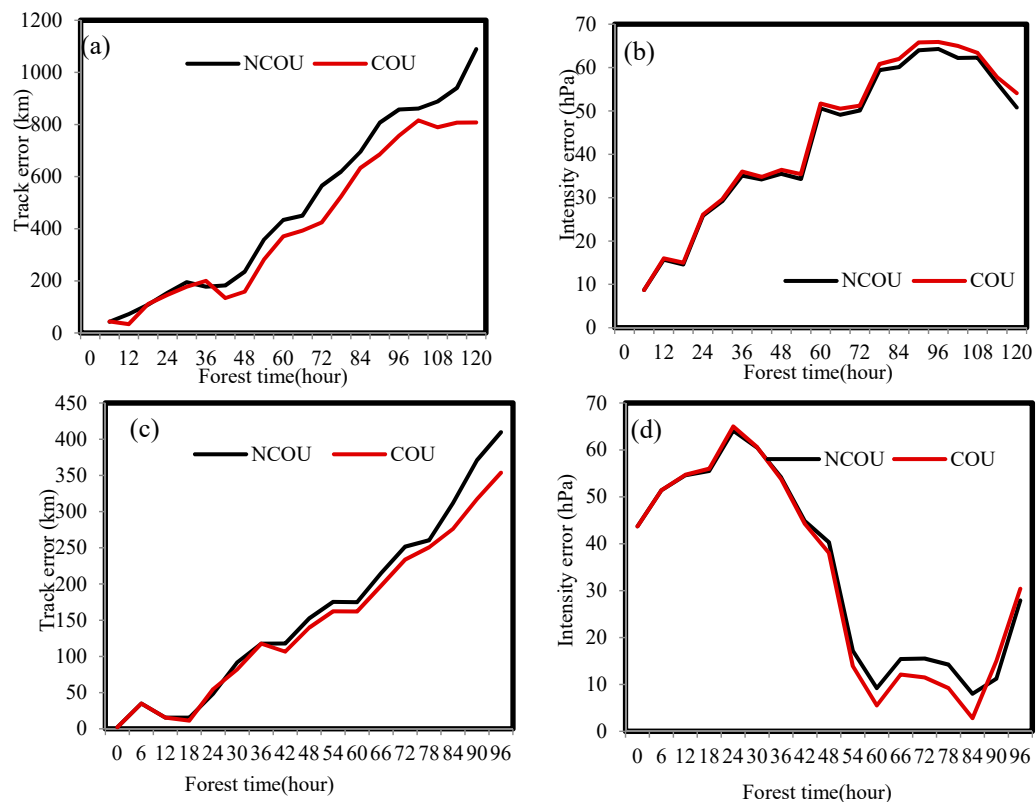
#### 4.3. Impacts on Typhoons

Based on the above analysis, pressure variables improved after coupling the  $T_s$  prognostic scheme. Therefore, the influence of this scheme on typhoons may be important.

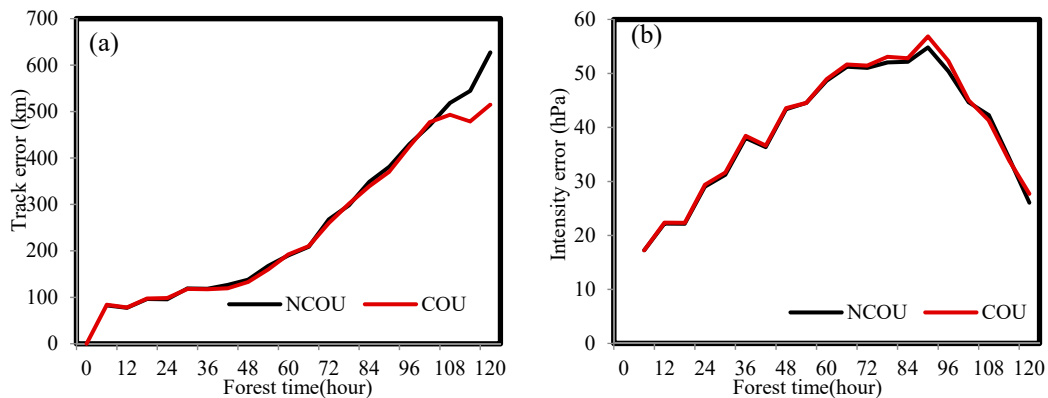
Here, we discuss six typhoon cases from 2016 with larger errors in the operational models. Typhoon Malakas (1616) and Typhoon Haima (1622) are selected as case studies. The typhoon cases with nine forecasting times are composited to analyze the impact of this scheme on them. The samples include simulations of Typhoon Nepartak (1601) at 08:00 and 20:00 on 3 July, Typhoon Meranti (1614) at 08:00 on 11 September, Typhoon Malakas (1616) at 08:00 on 13 September, Typhoon Megi (1617) at 08:00 on 23 September, Typhoon Chaba (1618) at 08:00 and 20:00 on 30 September, and Typhoon Haima (1622) at 20:00 on 17 October and at 08:00 on 18 October. The forecasting lead time for all samples is approximately 120 h, except for the 1622 “Hama” typhoon with 96 forecasting lead times. The configuration of the model simulation is identical to the two previous subsections.

Figure 11 provides the track and intensity errors from NCOU and COU experiments on Typhoons Malakas and Haima. Based on the track errors of the two typhoons (Figure 11a,c), the errors in the COU are smaller than those in the NCOU for the 0–120 forecast lead time, especially at longer forecasting lead times, the effect of improvement is slightly better. For example, the track error for the 48th forecast lead time from Typhoon Malakas in the NCOU is 235.658 km while that in the COU is 158.87 km. Based on the tracks of the two typhoons (Figures are omitted), the velocity in the COU is faster than that in the NCOU and closer to the observation. The reasons may be that the accuracy of forecasted environmental variables (such as temperature, specific humidity and wind) is improved and the steering flow on the west side of the subtropical high is more accurately described after coupling the  $T_s$  prognostic scheme in the model. Comparing the intensity errors for the two typhoons (Figure 11b,d), the errors for the two experiments are slightly different, where the errors for Typhoon Malaks in the COU are slightly larger than that in the NCOU and the errors for Typhoon Haima in the COU are smaller than in the NCOU. These may be related to the smaller diurnal variation of  $T_s$  from the COU during the period of the typhoon, which induced the small difference of  $T_s$  as well as the heat flux between the NCOU and the COU. The heat flux is an important factor influencing the intensity of a typhoon and, therefore, the intensity differences between the two are insignificant.

Figure 12 shows the average errors for the track and intensity of six typhoons in the two experiments. The average track errors (Figure 12a) for the COU are smaller than those in the NCOU after hour 36: the advantages in terms of the COU are relatively obvious with the increasing forecast lead times. The intensity errors for the two experiments are similar and the difference is unobvious (Figure 12b). The reasons are similar to the cases.



**Figure 11.** Errors for the track (a) and intensity (c) for the 1616 “Malakas” typhoon and (b,d), for the 1622 “Haima” typhoon.



**Figure 12.** Average errors for the track and intensity from six typhoons: (a) track and (b) intensity errors.

## 5. Discussion and Conclusions

Offline diagnostics of the  $T_s$  scheme show that the forecasted  $T_s$  is sensitive to the profile shape parameter  $\nu$  and the initial temperature  $T_b$ . Comparing with the observed  $T_s$  in this paper, the forecasted  $T_s$  is relatively reasonable when  $\nu$  is 0.2, which is different from that found by previous researchers ( $\nu = 1.0$  from Fairall et al. [1] and  $\nu = 0.3$  from Zeng et al. [12]). Because the  $\Delta T_w$  is restricted to about 3 K [1],  $\nu = 0.2$  is more suitable when the peak of solar radiation from coastal observed site exceeds  $1000 \text{ W/m}^2$ . Usually,  $T_b$  is taken as the ocean bulk temperature [1,9,32] or climatological SST [13], for which diurnal variation is small. Therefore,  $T_b$  is taken as the averaged  $T_s$  with little diurnal variation instead of bulk SST (without observed SST in offline diagnostics), and then, the forecasted  $T_s$  is reasonable.

The forecasted  $T_s$  of the CMA-TRAMS model after coupling the TS scheme presented a diurnal variation that was different from the fixed  $T_s$  of the uncoupled model. From 24-h to 120-h forecasted  $T_s$  every day during a month, there is a certain difference of  $T_s$  in those days influenced by an obvious synoptic system such as typhoons, between uncoupled and coupled models. The track errors of the typhoon decrease after 36-h forecasting, which may be caused by the more accurate forecast of steering flow on the west side of the subtropical high in the coupled model. However, the intensity errors between the two are similar. These could be related to the small difference of  $T_s$  as well as the heat flux between uncoupled and coupled models due to the smaller diurnal variation of  $T_s$  from the coupled model during the period of the typhoon.

Finally, three parameters of the  $T_s$  scheme are tested using the observed data of a typhoon not happening, which may be different from typhoon periods. However, it is very difficult to collect the observation from Bohe Base during the typhoon period at present. In future, the observation of typhoons should be applied to the offline diagnostics of the  $T_s$  scheme. The observed TS will be gained to compare it with the forecasted TS from the coupled model.

In addition, the models of CMA-TRAMS and the Hybrid Coordinate Oceanic Model (HYCOM) will be coupled and compared with the model of the coupling  $T_s$  scheme. The results could provide some basis for the better application of the  $T_s$  scheme in the CMA-TRAMS.

**Author Contributions:** Conceptualization, Z.C. and W.M.; methodology, Y.Z.; formal analysis, D.X.; validation, Z.C. and W.M.; writing—original draft preparation, Y.Z.; writing—review and editing, Y.Z. All authors have read and agreed to the published version of the manuscript.

**Funding:** This paper is Supported by National Key R & D Program of China (2018YFC1506902); National Natural Science Foundation of China (42175105; U2142213); Guangdong Basic and Applied Basic Research Foundation (2022A1515011870).

**Acknowledgments:** We specially thank to the crew of the Marine Meteorological Science Experiment Base at Bohe for their help in conducting the field program and providing the observed data of offline diagnostics.

**Conflicts of Interest:** The authors declare no conflict of interest.

## References

1. Fairall, C.W.; Bradley, E.F.; Godfrey, J.S.; Wick, G.A.; Edson, J.B.; Young, G.S. Cool-skin and warm-layer effects on sea surface temperature. *J. Geophys. Res.* **1996**, *101*, 1295–1308. [[CrossRef](#)]
2. Donlon, C.; Robinson, I.; Casey, K.S.; Vazquez-Cuervo, J.; Armstrong, E.; Arino, O.; Gentemann, C.; May, D.; LeBorgne, P.; Piollé, J.; et al. The global ocean data assimilation experiment high-resolution sea surface temperature pilot project. *Bull. Am. Meteorol. Soc.* **2007**, *88*, 1197–1213. [[CrossRef](#)]
3. Kawai, Y.; Wada, A. Diurnal sea surface temperature variation and its impact on the atmosphere and ocean: A review. *J. Oceanogr.* **2007**, *63*, 721–744. [[CrossRef](#)]
4. Webster, P.J.; Clayson, C.A.; Curry, J.A. Clouds, radiation, and the diurnal cycle of sea surface temperature in the tropical western Pacific. *J. Clim.* **1996**, *9*, 1712–1730. [[CrossRef](#)]
5. Llewellyn-Jones, D.T.; Minnett, P.J.; Saunders, R.W.; Zavody, A.M. Satellite multichannel infrared measurements of sea surface temperature of the NE Atlantic Ocean using AVHRR/2. *Q. J. R. Meteorol. Soc.* **1984**, *110*, 613–631. [[CrossRef](#)]
6. Murray, M.J.; Allen, M.R.; Merchant, C.J.; Harris, A.R.; Donlon, C.J. Direct observations of skin-bulk SST variability. *Geophys. Res. Lett.* **2000**, *27*, 1171–1174. [[CrossRef](#)]
7. Al-Shehhi, M.R. Uncertainty in satellite sea surface temperature with respect to air temperature, dust level, wind speed and solar position. *Reg. Stud. Mar. Sci.* **2022**, *53*, 102385. [[CrossRef](#)]
8. Clayson, C.A.; Curry, J.A. Determination of surface turbulent fluxes for the Tropical Ocean-Global Atmosphere Coupled Ocean Atmosphere Response Experiment: Comparison of satellite retrievals and in situ measurements. *J. Geophys. Res.* **1996**, *101*, 515–528. [[CrossRef](#)]
9. Gentemann, C.L.; Donlon, C.J.; Stuart-Menteth, A.; Wentz, F.J. Diurnal signals in satellite sea surface temperature measurements. *Geophys. Res. Lett.* **2003**, *30*, 1140. [[CrossRef](#)]
10. Zeng, X.; Zhao, M.; Dickinson, R.E.; He, Y. A multi-year hourly sea surface skin temperature dataset derived from the TOGA TAO bulk temperature and wind speed over the tropical Pacific. *J. Geophys. Res.* **1999**, *104*, 1525–1536. [[CrossRef](#)]
11. Beljaars, A.C.M. Air-sea interaction in the ECMWF model. In Proceedings of the Seminar on Atmosphere-Surface Interactions, Reading, UK, 8–12 September 1997; Eur. Cent. for Med. Range Weather Forecasts: Reading, UK, 1997.

12. Zeng, X.; Beljaars, A. A prognostic scheme of sea surface skin temperature for modeling and data assimilation. *Geophys. Res. Lett.* **2005**, *32*, L14605. [[CrossRef](#)]
13. Brunke, M.A.; Zeng, X.; Misra, V.; Beljaars, A. Integration of a prognostic sea surface skin temperature scheme into weather and climate models. *J. Geophys. Res.* **2008**, *113*, D21117. [[CrossRef](#)]
14. Takaya, Y.; Bidlot, J.-R.; Beljaars, A.C.M.; Janssen, P.A.E.M. Refinements to a prognostic scheme of skin sea surface temperature. *J. Geophys. Res.* **2010**, *115*, C06009. [[CrossRef](#)]
15. Shelly, A.; Xavier, P.; Copsey, D.; Johns, T.; Rodríguez, J.M.; Milton, S.; Klingaman, N. Coupled versus uncoupled hindcast simulations of the Madden–Julian Oscillation in the year of tropical convection. *Geophys. Res. Lett.* **2014**, *41*, 5670–5677. [[CrossRef](#)]
16. Perlin, N.; Kamenkovich, I.; Gao, Y.; Kirtman, B.P. A study of mesoscale air–sea interaction in the Southern Ocean with a regional coupled model. *Ocean Model.* **2020**, *153*, 101660. [[CrossRef](#)]
17. Valdivieso, M.; Peatman, S.C.; Klingaman, N.P. The influence of air–sea coupling on forecasts of the 2016 Indian summer monsoon and its intraseasonal variability. *Q. J. R. Meteorol. Soc.* **2020**, *147*, 202–228. [[CrossRef](#)]
18. Smith, G.C.; Bélanger, J.-M.; Roy, F.; Pellerin, P.; Ritchie, H.; Onu, K.; Roch, M.; Zadra, A.; Colan, D.S.; Winter, B.; et al. Impact of coupling with an ice–ocean model on global medium-range NWP forecast skill. *Mon. Weather Rev.* **2018**, *146*, 1157–1180. [[CrossRef](#)]
19. Browne, P.A.; de Rosnay, P.; Zuo, H.; Bennett, A.; Dawson, A. Weakly coupled ocean–atmosphere data assimilation in the ECMWF NWP system. *Remote Sens.* **2019**, *11*, 23. [[CrossRef](#)]
20. Vellinga, M.; Copsey, D.; Graham, T.; Milton, S.; Johns, T. Evaluating benefits of two-way ocean–atmosphere coupling for global NWP forecasts. *Weather Forecast.* **2020**, *35*, 2127–2144. [[CrossRef](#)]
21. Roberts, C.D.; Vitart, F.; Balmaseda, M.A.; Molteni, F. The time-scale-dependent response of the wintertime North Atlantic to increased ocean model resolution in a coupled forecast model. *J. Clim.* **2020**, *33*, 3663–3689. [[CrossRef](#)]
22. Patoux, J.; Kelly, K.A. Sensitivity of midlatitude storm intensification to perturbations in the sea surface temperature near the Gulf Stream. *Mon. Weather Rev.* **2012**, *140*, 1241–1256.
23. Crnivec, N.; Smith, R.K.; Kilroy, G. Dependence of tropical cyclone intensification rate on sea-surface temperature. *Q. J. R. Meteorol. Soc.* **2016**, *142*, 1618–1627. [[CrossRef](#)]
24. Khan, M.Z.K.; Sharma, A.; Mehrotra, R. Global seasonal precipitation forecasts using improved sea surface temperature predictions. *J. Geophys. Res. Atmos.* **2017**, *122*, 4773–4785. [[CrossRef](#)]
25. Seroka, G.; Miles, T.; Xu, Y.; Kohut, J.; Schofield, O.; Glenn, S. Rapid shelf-wide cooling response of a stratified coastal ocean to hurricanes. *J. Geophys. Res. Ocean.* **2017**, *122*, 4845–4867. [[CrossRef](#)] [[PubMed](#)]
26. Schadea, L.R.; Emanuel, K.A. The ocean’s effect on the intensity of tropical cyclones: Results from a simple coupled atmosphere-ocean model. *J. Atmos. Sci.* **1999**, *56*, 642–651. [[CrossRef](#)]
27. Jiang, X.P.; Liu, C.X.; Qi, Y.Q. The simulation of Typhoon Krovanh using a coupled air-sea model. *Chin. J. Atmos. Sci.* **2009**, *33*, 99–108.
28. Wu, Z.; Jiang, C.B.; Deng, B.; Chen, J.; Long, Y.N.; Qu, K.; Liu, X.J. Numerical investigation of Typhoon Kai-tak (1213) using a mesoscale coupled WRF-ROMS model. *Ocean. Eng.* **2019**, *175*, 1–15. [[CrossRef](#)]
29. Zhao, X.; Chan, J.C.L. Changes in tropical cyclone intensity with translation speed and mixed-layer depth: Idealized WRF-ROMS coupled model simulations. *Q. J. R. Meteorol. Soc.* **2017**, *143*, 152–163. [[CrossRef](#)]
30. Heo, K.Y.; Ha, T.; Park, K.S. The effects of a typhoon-induced oceanic cold wake on typhoon intensity and typhoon-induced ocean waves. *J. Hydro-Environ. Res.* **2017**, *14*, 61–75. [[CrossRef](#)]
31. Sun, J.; Li, J.; Ruan, Z.X.; Wu, K.; Li, F.Z. Simulation study on the effect of atmosphere-ocean-wave interactions on Typhoon Rammasun (2014) in the South China Sea. *J. Atmos. Sol.-Terr. Phys.* **2021**, *212*, 105490. [[CrossRef](#)]
32. Lim Kam Sian, K.T.C.; Dong, C.; Liu, H.; Wu, R.; Zhang, H. Effects of Model Coupling on Typhoon Kalmaegi (2014) Simulation in the South China Sea. *Atmosphere* **2020**, *11*, 32. [[CrossRef](#)]
33. ECMWF. Physical Processes, IFS DOCUMENTATION – Cy47r3 Operational Implementation. Available online: <https://www.ecmwf.int/sites/default/files/elibrary/2007/9224-part-vii-ecmwf-wave-model.pdf> (accessed on 12 October 2021).
34. Wick, G.A.; Ohlmann, J.C.; Fairall, C.W.; Jessup, A.T. Improved oceanic cool skin correlation using a refined solar penetration model. *J. Phys. Oceanogr.* **2005**, *35*, 1986–1996. [[CrossRef](#)]
35. Large, W.G.; McWilliams, J.C.; Doney, S.C. Oceanic vertical mixing: A review and a model with a nonlocal boundary layer parameterization. *Rev. Geophys.* **1994**, *32*, 363–403. [[CrossRef](#)]
36. Chen, Z.T.; Dai, G.F.; Luo, Q.H.; Zhong, S.X.; Zhang, Y.X.; Dao-Sheng, X.U.; Huang, Y.Y. Study on the coupling of model dynamics and physical processes and its influence on the forecast of typhoons. *J. Trop. Meteorol.* **2016**, *32*, 1–8.
37. Xu, D.S.; Zhang, Y.X.; Wang, G. Improvement of Meso-Sas cumulus parameterization scheme and its application in a model of 9 km resolution. *J. Trop. Meteorol.* **2015**, *31*, 608–618.
38. Chen, Z.T.; Dai, G.F.; Zhong, S.X.; Huang, Y.; Zhang, Y.; Xu, D.; Li, M. Technical features and prediction performance of typhoon model for the South China Sea. *J. Trop. Meteorol.* **2016**, *32*, 831–840.
39. Zhang, Y.X.; Chen, Z.; Meng, W.; Xu, D.S. Applicability of temperature discrete equation to NMRF boundary layer scheme in GRAPES model. *J. Trop. Meteorol.* **2022**, *28*, 12–28.
40. Zhong, S.X.; Chen, Z.T.; Dai, G.F. Impacts of orographic gravity wave drag parameterization on typhoon intensity and path forecasting. *Chin. J. Atmos. Sci.* **2014**, *38*, 273–284.

41. Xu, D.S.; Chen, Z.T.; Zhong, S.X.; Dai, G.F. Study of the coupling of cumulus convection parameterization with cloud microphysics and its influence on forecast of typhoon. *Acta Meteorol. Sin.* **2014**, *72*, 337–349.
42. Dai, G.F.; Chen, Z.T. Sensitive experiments of the surface flux on a simulated typhoon in grapes. *J. Trop. Meteorol.* **2013**, *29*, 403–410.
43. Huang, J.; Chan, P. Progress of marine meteorological observation experiment at Maoming of South China. *J. Trop. Meteor.* **2011**, *17*, 418–429.
44. Huang, H.J.; Mao, W.K. The South China sea monsoon experiment—Boundary layer height (SCSMEX-BLH): Experimental design and preliminary results. *Mon. Wea. Rev.* **2015**, *143*, 5035–5053. [[CrossRef](#)]